water

MDPI

Article

Research on Flow Field Characteristics of a Three-Plate Vertical Rotary Gate

Houyi Qi [1], Xiao Zhang [1,2,3,*], Yuxue Sun [1], Xinyu Ji [1], Dong Tian [3], Chao Sun [3], Zhenzhen Xue [3] and Yanshun Liu [1,*]

[1] Institute of Geotechnical and Underground Engineering, Shandong University, Jinan 250061, China; 201920539@mail.sdu.edu.cn (H.Q.)
[2] Laoshan Laboratory, Qingdao 266200, China
[3] Shandong Fangneng New Growth Drivers Institute Co., Ltd., Weifang 261200, China; xixixiao2018@163.com (Z.X.)
* Correspondence: sduzhangxiao@sdu.edu.cn (X.Z.); 202014974@mail.sdu.edu.cn (Y.L.)

Abstract: Steady-state and transient hydraulic characteristics of a novel three-plate vertical rotary gate were analysed through physical model experiments and numerical simulations. An experimental gate system was built to analyse the flow characteristics of the gate, and a steady-state flow prediction model was proposed. Steady-state numerical simulations of the gate were conducted to analyse flow field distribution characteristics. A transient numerical model of the gate was established to analyse the flow field distribution characteristics during opening and closing. The discharge coefficient evolution law under different speed conditions was revealed. Under various water levels, the steady-state discharge coefficient of the gate was similar. Within a 0–90° opening, the discharge coefficient grew exponentially. A steady-state flow prediction model for the gate revealed a prediction error of <7%. The discharge coefficient of the gate increased with decreasing opening speed; when the gate was closed, it exhibited asymmetric variation characteristics. The flow hysteresis effect was more evident at higher speeds. Plate 2 experienced the maximum flow force. In the transient state, the flow force acting on the plates exhibited a periodic fluctuation pattern, and the maximum flow force increased with the gate speed. A reference for the design and application of fast opening and closing gates is provided.

Keywords: sluice gate; flow field characteristics; steady-state and transient simulation; discharge coefficient; flow prediction model

check for updates

Academic Editor: Giuseppe Pezzinga

Received: 30 December 2024
Revised: 2 February 2025
Accepted: 4 February 2025
Published: 6 February 2025

Citation: Qi, H.; Zhang, X.; Sun, Y.; Ji, X.; Tian, D.; Sun, C.; Xue, Z.; Liu, Y. Research on Flow Field Characteristics of a Three-Plate Vertical Rotary Gate. *Water* **2025**, *17*, 456. https://doi.org/10.3390/w17030456

1. Introduction

A sluice gate is an important component of hydraulic structures that can be used to intercept water flow, control water levels, regulate flow rate, and discharge sediment and floating debris. There are several types and classifications of gates, and different gate types are suitable for various engineering conditions. According to their structural form, gates can be divided into plane [1–3], radial [4–6], mitre [7,8], arched [9,10], and sector [11,12] gates. However, these gates can only be opened and closed under static water conditions or at a slower speed under dynamic water conditions to ensure their stability and safety during operation [13–17]. Currently, there is no research on gates that can be opened or closed quickly or periodically.

The study of flow field characteristics is crucial for the design and safe operation of gates. Many scholars have conducted studies on the steady-state flow fields of gates using methods such as prototype observation experiments, physical model experiments, and numerical simulations. Bijankhan [18] improved the original gate flow formula of Ferro [19] and Shahrokhnia [20] using dimensional analysis and the incomplete self-similarity theory based on flume experimental data. Marashi [21,22] analysed the relationship between the flow rate of a semicircular rotary gate and the water level in front of the gate, gate opening, and submergence depth through model experiments. In addition, a flow calculation formula for semicircular rotary gates was established. Norouzi [23] studied the influence of gate sills with varying shapes and widths on the vortices near sluice gates. Elgamal [24] proposed setting a rotor upstream of the gate to control the upstream water level and analysed the hydraulic performance of gates with different rotor shapes. Kim [25] and Jung [26] used Flow-3D to establish large-scale three-dimensional water gate models for the Changnyeong–Haman and Saemangeum tidal dikes, respectively. They comprehensively analysed the hydraulic characteristics of the downstream section of the water gate, such as the average flow velocity and maximum flow velocity at the bottom, under various working conditions, and evaluated the operation status of the water gate. Shen [27] used numerical methods to simulate the unstable flow of a plane gate and predicted the three-dimensional flow field in the vicinity of the plane gate with a submerged discharge. Daneshfaraz [28,29] used FLOW-3D software (edition 11 version 2) to study the effect of integration on the flow field of labyrinth sluice gates and provided a general formula for calculating the discharge coefficient through gates with various sill states. Gül [30] used Reynolds-averaged Navier–Stokes (RANS) equations with the volume of fluid (VOF) and k-epsilon turbulence models to numerically simulate a sluice gate and analysed the influence of variable-sized energy-dissipating blocks on the flow field of the sluice gate. Yan [31] proposed a convolutional neural network (CNN) to predict the flow field around a sluice gate. Daneshfaraz [32] simulated the influence of the geometric shape and sill size on the flow field of a sluice gate. Rentachintala [33] developed a generalised equation for the elementary discharge coefficient of a skew side sluice gate both for free and submerged flow conditions and evaluated the discharge characteristics of the skew side sluice gate. Meng [34] studied a novel trapezoidal sluice gate designed for water division and flow control within irrigation networks featuring canals with trapezoidal cross-sections.

Some scholars have also researched the transient flow fields of gates. Wang [35] investigated the hydraulic characteristics of a vertical U-shaped gate under varying flow rates and gate openings through model testing cooperating with numerical simulation and analysed the hydraulic evolution process. Shen [36] used the VOF model and large eddy simulation (LES) method to successfully capture the transient turbulent characteristics of flow under different water flow conditions and analysed the influence of opening on the vortex structure characteristics near the gate. Takagi [37] studied the effect of the opening speed of the gate on a dam break and found that the gate speed affected the jet volume and pressure near the gate. Based on the RNG k-epsilon turbulence model, Li [38] studied the influence of the gate closing speed and control amplitude on the water flow movement in a pool and the hydraulic characteristics of the pressure tunnel during the gate control process. They provided reference suggestions for the safe operation and emergency control of water distribution hub projects. Zhang [39] conducted three-dimensional numerical simulations of a transient flow field during the opening and closing processes of gates with different bottom-edge forms. Currently, research on the flow field characteristics of gates mainly focuses on the steady-state flow field at different opening degrees, and there is relatively little research on the transient flow field characteristics of gates at different opening and closing speeds.

In this study, a new type of gate was designed for a scenario that requires rapid opening and closing of the gate. First, physical model experiments were conducted on the gate, and a steady-state flow prediction model was established. Subsequently, a steady-state numerical simulation was conducted on the hydraulic characteristics of the gate at different openings using a steady-state model, and the evolution laws of the pressure, flow velocity, and dynamic hydraulic force of the gate in the flow field were analysed. Finally, transient numerical simulation methods were used to study the transient flow field characteristics during the opening and closing processes of the gate. Considering the different opening and closing speeds of the gate, a variation curve of the discharge coefficient during the gate opening and closing processes was established. By analysing the hydraulic characteristics near the gate under different operating conditions and the changes in the flow force during the gate opening and closing processes, reliable references can be provided for future similar engineering applications.

2. Materials and Methods

2.1. Design of Three-Plate Vertical Rotary Gate

A novel three-plate vertical rotary gate was designed and developed, and the structure is illustrated in Figure 1. The plates are connected to the main structure using bearings, seals, and shafts; furthermore, they are connected to a motor through a shaft, gears, and couplings, and rotate using the motor. The number of plates was set based on the width of the water channels. The total size of the internal section of the gate was 0.3 × 0.2 m. To reduce the force on the plates during rotation, three plates were set with a size of 0.1 × 0.2 × 0.005 m. The gate simultaneously controlled multiple plates to open and close differentially to regulate system flow during operation. The gate opened and closed once every 0.9 s, with the characteristic of fast response. When the gate was opened and closed, the hydrodynamic load was evenly distributed on each plate; thus, the operating force of the gate was relatively small.

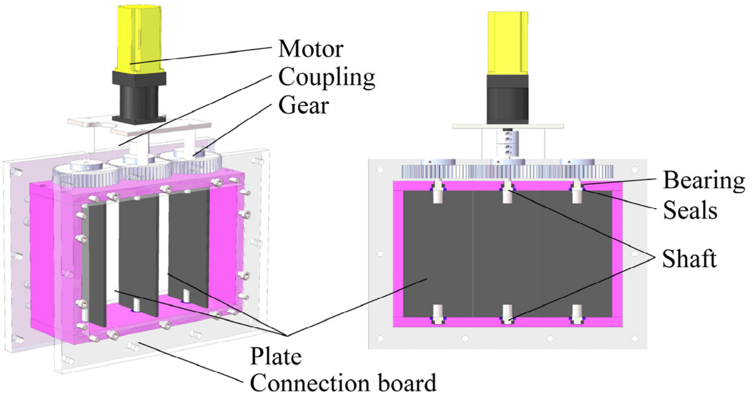

Figure 1. Structure of three-plate vertical rotary gate.

2.2. Experimental Setup

An experimental system was constructed and tested to study the flow characteristics of the new gate type. The experimental system included a constant-pressure water tank, water channel, rotary gate, flume, lower water tank, electromagnetic flowmeter, centrifugal pump, and pipelines. The layout of the experimental setup is shown in Figure 2.

The water channel was fabricated from organic glass for easy observation of water flow patterns. The length of the channel was 3.0 m, and the cross-sectional size of the gate section was 0.3 × 0.2 m. A rotary gate was placed inside the water channel. The water channel inlet was a constant-pressure water tank, and an overflow device was installed next to the water tank to control the water level. A flat gate was installed inside the water tank to control the conduction and cessation of the experiments. The flume was the outlet of the water channel. The constant pressure water tank and flume were equipped with water-level sensors to monitor the water-level height in real time. The end of the flume was equipped with an overflow plate that maintained the water level in the flume. Water in the lower tank was circulated through the pipeline to a constant-pressure water tank. The installation of an electromagnetic flowmeter and a centrifugal pump in the return water pipeline can achieve real-time flow monitoring and control in the experimental system.

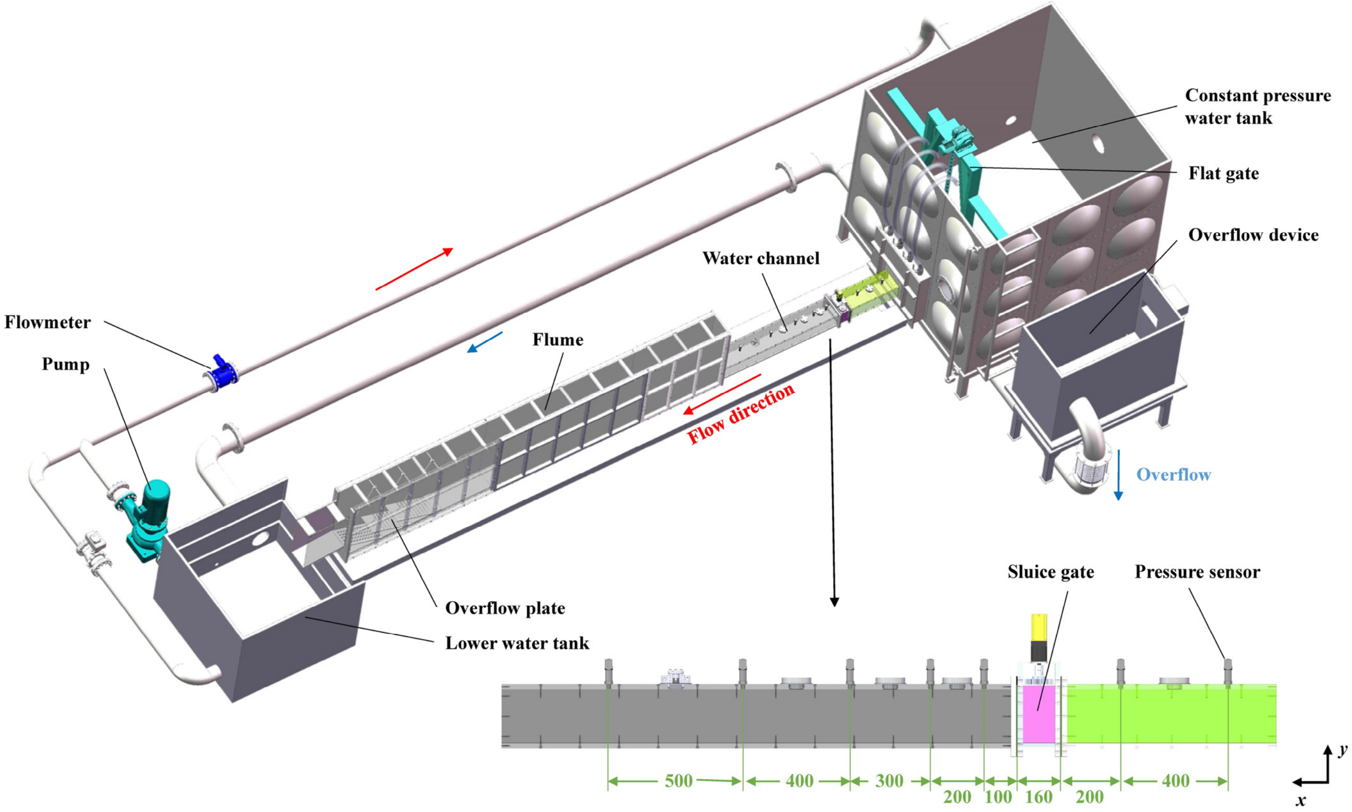

Figure 2. Composition of the experimental system.

The water channel was located at the core of the experimental system. Seven measuring points were arranged along the centreline of the water channel roof. Owing to the overall stability of the pressure distribution upstream of the gate and the complexity of the pressure distribution downstream of the gate, two and five monitoring points were established in front of and behind the gate, respectively. The specific installation method for the pressure sensors is shown in Figure 2. The pressure sensor model was SUP-P300, with a range of 0–20 kPa and an accuracy of 0.5% F.S. The model of the electromagnetic flowmeter was BTLD-250TB, with a maximum range of 880 m^3/h and an accuracy of 0.5% F.S.

Appropriate upstream and downstream water level heights were selected based on the experimental site conditions. In the experiment, the gate opening was defined as the angle at which Plate 2 of the gate rotated. The range of gate opening was 0–180°. The gate plates operated in the opening process between 0–90° and in the closing process between 90–180°. In the experiment, the gate opening range was set to 10–90°. The upstream water level was controlled using a constant-pressure water tank. The water level range was set to ~1.0–1.6 m, with a total of 4 experimental groups. The downstream water level was regulated and controlled using the overflow plate, and the water level remained constant at 0.4 m during the experiment. Because the bottom of the water tank and the bottom of the flume were not at the same height (with a height difference of 0.35 m), the actual water level difference in the experiment was ~0.25–0.85 m. The test conditions and parameters are listed in Table 1.

Table 1. Experimental plan.

Group of Working Conditions	Water Level of the Water Tank H_1/m	Submergence Depth of the Flume H_2/m	Actual Water Level Difference ΔH/m	Opening Degree of the Gate θ/°
1	1.0	0.4	0.25	10, 20, 30, 40, 50, 60, 70, 80, 90
2	1.2	0.4	0.45	
3	1.4	0.4	0.65	
4	1.6	0.4	0.85	

The experimental steps of this study were as follows:

(1) Instrument calibration was performed at the beginning of the experiment. When the water level stabilised, the readings from the water tank level gauge, electromagnetic flowmeter, and pressure sensor were calibrated separately.

(2) When the constant-pressure water tank reached the set water level, the flat gate and variable centrifugal pump were opened.

(3) A control system was used to control the opening of the gate and adjust it to the required opening for the experiment.

(4) The overflow device and centrifugal pumps were adjusted to ensure that the upstream and downstream water levels satisfied the test conditions. The experimental measurements commenced.

(5) The upstream water level and gate opening were adjusted separately, and steps (1)–(4) were repeated.

When the upstream water level and gate opening were adjusted each time, the flow rate in the system was maintained at a stable level by adjusting the overflow and centrifugal pumps. Experiments were conducted sequentially according to different gate openings and water-level differences. Data from the pressure sensor and electromagnetic flowmeter were recorded only after the readings of the electromagnetic flowmeter stabilised during each experiment. At least three sets of each operating condition were repeated, and the average was considered as the test result.

2.3. Numerical Simulation

2.3.1. Governing Equations

Numerical simulations were conducted to investigate the distribution characteristics of the flow field near the gate. Water was used as the medium in the water channel and was an incompressible viscous fluid. Without considering heat exchange during the flow process, the continuity and momentum equations used in the numerical simulation calculations were as follows:

$$\frac{\partial u_i}{\partial x_i} = 0, \tag{1}$$

$$\frac{\partial(\rho u_i)}{\partial t} + \frac{\partial(\rho u_i u_j)}{\partial x_i} = -\frac{\partial p}{\partial x_i} + \mu \frac{\partial^2 u_i}{\partial x_i \partial x_j} + \rho F_i, \tag{2}$$

where u_i and u_j are the instantaneous values of the flow velocity in the i and j directions, respectively; x_i and x_j are the coordinates; ρ is the fluid density; p is the fluid pressure; μ is the dynamic viscosity; F_i is the mass force.

The flow near the gate is complex and prone to complex turbulence phenomena such as flow separation. The gate wall had a significant impact on the nearby flow, requiring high requirements for a boundary-layer mesh. Therefore, the SST k—ω model was used for solving and calculating [40–43] as follows:

$$\frac{\partial}{\partial t}(\rho k) + \frac{\partial}{\partial x_i}(\rho k u_i) = \frac{\partial}{\partial x_j}\left[\Gamma_k \frac{\partial k}{\partial x_j}\right] + \widetilde{G}_k - Y_k + S_k, \tag{3}$$

$$\frac{\partial}{\partial t}(\rho \omega) + \frac{\partial}{\partial x_i}(\rho \omega u_i) = \frac{\partial}{\partial x_j}\left[\Gamma_\omega \frac{\partial \omega}{\partial x_j}\right] + G_\omega - Y_\omega + D_\omega + S_\omega, \tag{4}$$

where Γ_k and Γ_ω represent the effective diffusivity of k and ω, respectively; $\widetilde{G}_k$ represents the generation of turbulence kinetic energy due to mean velocity gradients; Y_k and Y_ω represent the dissipation of k and ω due to turbulence, respectively; S_k and S_ω are user-defined source terms; G_ω represents the generation of ω; D_ω represents the cross-diffusion term.

2.3.2. Establishment of Numerical Models

Typically, vortices exist in the flow field behind the gate, and the flow field is more complex. The upstream length of the sluice gate was set to approximately five times that of the gate width, whereas the downstream length was approximately 10 times that of the gate width. The three-dimensional model of the water channel and sluice gate is shown in Figure 3.

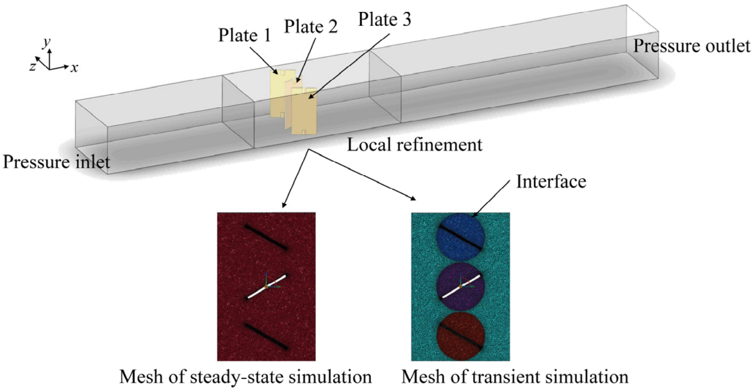

Figure 3. Schematic diagram of geometric model and mesh partition.

Considering the complexity of the computational domain structure, polyhedral grids were used for all regions. For the steady-state simulation, the flow on the surface and behind the gate was relatively complex; therefore, the local refinement method was adopted to capture the turbulent phenomena. A sliding mesh was used for the transient simulation, and the mesh of the interface was locally refined.

Flow rate, pressure, and flow rates at the inlet and outlet of the monitoring model were monitored. The x-z section at the centre of the water channel was selected as the observation section for the flow field changes. The flow velocity and pressure parameters of the left, middle, and right longitudinal profiles of the x-z sections were monitored, as shown in Figure 4. Simultaneously, the flow forces acted on the walls of Plates 1, 2, and 3 in the x-axis direction.

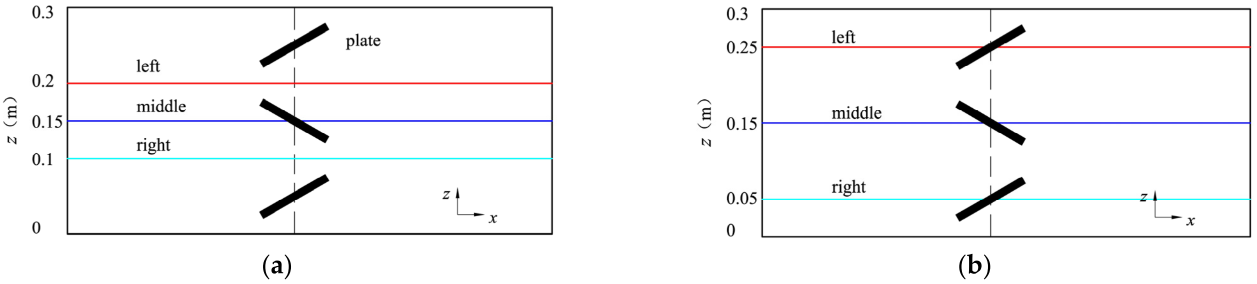

Figure 4. Location profile of monitoring line. (**a**) Flow rate monitoring line and (**b**) pressure monitoring line.

2.3.3. Numerical Simulation Scheme

(1) Steady-state simulation scheme

In the steady-state simulation, room temperature (20 °C) water was used as the fluid medium. Nine gate openings were simulated.

In the physical model experiment, different pressure boundary conditions were set to characterise the different water levels in the water tank and the submergence depth of the flume (the water head was taken as the height from the centre of the water channel to the water surface). In the experiment, the distances between the centre of the channel and the height of the water tank and flume were 0.45 and 0.1 m, respectively. The specific operating conditions are listed in Table 2.

Table 2. Operating conditions of steady-state simulation.

Working Condition Group	Water Level of the Water Tank /m	Submergence Depth of the Flume/m	Actual Water Level Difference ΔH/m	Inlet Pressure/kPa	Outlet Pressure/kPa	Opening Degree of the Gate Θ/°
1	0.9	0.4	0.15	4.41	2.94	10°, 20°, 30°, 40°, 50°, 60°, 70°, 80°, 90°
2	1	0.4	0.25	5.39	2.94	
3	1.1	0.4	0.35	6.37	2.94	
4	1.2	0.4	0.45	7.35	2.94	
5	1.3	0.4	0.55	8.33	2.94	
6	1.4	0.4	0.65	9.31	2.94	
7	1.5	0.4	0.75	10.29	2.94	
8	1.6	0.4	0.85	11.27	2.94	

Working conditions with a gate opening of 50° and a water level difference of 0.85 m were selected for mesh independence verification. The grid sizes of the local refinement area were 8, 4, and 2 mm. Numerical models with grids 50, 200, and 800 w were obtained. The magnitudes of the flow velocities after the convergence calculation were compared. The error in the calculation results for grids the 200 and 800 w grids was only 0.14%. The error in the calculation results for the grids of 50 and 800 w was 2.7%. Therefore, using a 200 w grid for steady-state calculations ensured the accuracy of the calculation results.

(2) Transient simulation scheme

During transient simulation, five gate rotation speeds of 200, 100, 50, 25, and 12.5°/s were selected for simulation. The calculation duration was the time required for the plate to rotate once or for the gate to open and close twice. The remaining boundary conditions of the model were consistent with those of the steady-state simulation. The operating conditions are listed in Table 3.

Table 3. Operating conditions of transient simulation.

Working Condition Group	Inlet Pressure/kPa	Outlet Pressure/kPa	Rotational Speed/deg·s^{-1}			Calculation Duration/s
			Plate 1	Plate 2	Plate 3	
1	11.27	2.94	200	−200	200	1.8
2			100	−100	100	3.6
3			50	−50	50	7.2
4			25	−25	25	14.4
5			12.5	−12.5	12.5	28.8

In the transient simulation, a working condition with a gate rotation speed of 200°/s was selected for grid independence verification. By changing the grid size, numerical models with grid sizes of 100, 200, and 600 w were obtained. The position and fluctuation errors of the maximum flow velocity were compared after convergence calculation. Comparing the positions of the maximum flow velocity in the two cycles, the maximum errors of 100 and 200 w compared to 600 w were 0.38% and 0.3%, respectively. Comparing the maximum flow velocity fluctuations obtained from the two cycles, it was found that there were fluctuation errors of 0.25%, 0.09%, and 0.06% in the maximum flow velocity when the numbers of grids were 100, 200, and 600 w, respectively. Therefore, considering both the computational cost and convergence, this study used a 200 w grid for transient simulation.

The operating conditions with a gate rotation speed of 200°/s were selected, and the time steps were set to 0.05, 0.01, 0.005, and 0.001 s, respectively, to verify time independence. When the time steps were set to 0.05, 0.01, and 0.005 s, the errors of the maximum flow velocity compared with the calculation result of 0.001 s reached 5.48%, 1.15%, and 0.23%, respectively. Therefore, the transient model used in this study was calculated with a time step of 0.005 s.

3. Results

3.1. Steady-State Flow Prediction Model

3.1.1. Analysis of Experimental Results

Based on the experimental results, the flow rate and pressure differential curves at different openings were drawn, as shown in Figure 5a. Under the same water-level difference, the flow rate in the water channel exhibited a non-linear increasing trend with an increase in the gate opening. Under different water level differences, the flow growth trend was approximately the same. Under the same water level difference, the pressure differential before and after the gate decreased as the gate opening increased. The decreasing trend of the pressure differential was approximately the same for different water-level differences. When the gate opening was <40°, changing the opening had a negligible effect on the pressure differential. At this point, the overall flow in the water channel was poor, which could easily result in significant energy loss.

Traditional flow calculation formulae were not applicable because of the special form of the gate. The gate was located inside a pressurised water channel, and the Bernoulli equation can be used to represent the relationship between pressure and flow velocity within the channel. Thus, the gate outflow characteristics were obtained. Two sections were used before and after the gate, with Section 1 at the inlet of the flow and Section 2 at the outlet. The flow at the cross-section must be smooth and satisfy the characteristics of gradient flow. The Bernoulli equation for the fluid is as follows:

$$\frac{P_1}{\rho g} + z_1 + \frac{v_1}{2g} = \frac{P_2}{\rho g} + z_2 + \frac{v_2}{2g} + h_w. \tag{5}$$

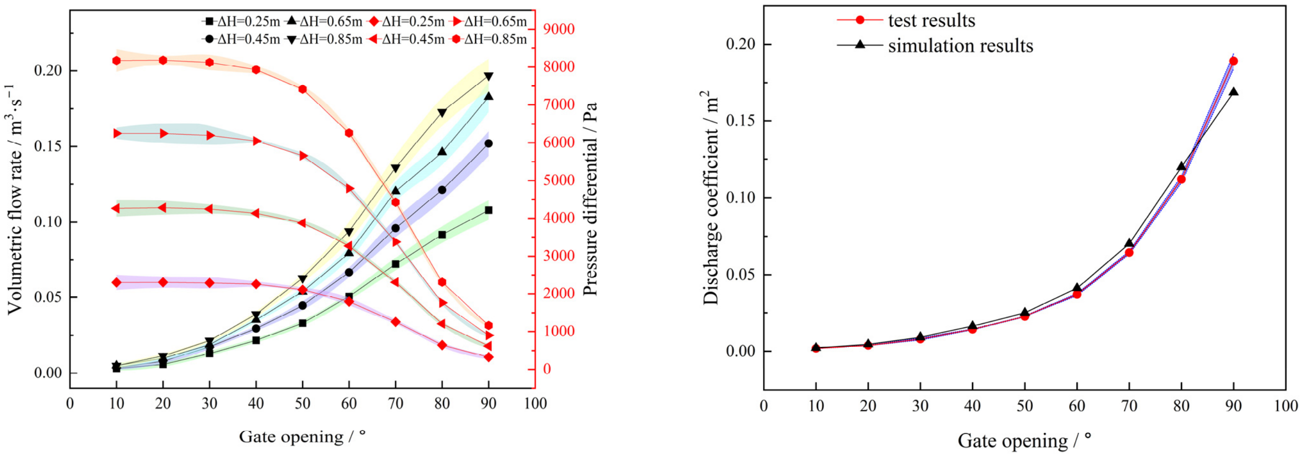

(**a**) (**b**)

Figure 5. Analysis of experimental results. (**a**) Flow rate and pressure differential at different gate openings, and (**b**) comparison of discharge coefficients.

In the actual flow process, the water channel was in a horizontal position, and the two cross-sectional areas before and after the gate were equal ($z_1 = z_1$ and $v_1 = v_1$). Ignoring the head loss throughout, the head loss between the two sections was $h_w = \sum \xi_c \frac{v^2}{2g}$. If the cross-sectional area of the water channel is taken as A, the flow formula in the channel is

$$Q = v \cdot A = \frac{A}{\sqrt{\sum \xi_c}} \sqrt{2\frac{\Delta P}{\rho}}, \tag{6}$$

where P_1 and P_2 are the pressure in Sections 1 and 2, respectively; v_1 and v_1 are the velocity in Sections 1 and 2, respectively; z_1 and z_1 are the height in Section 1 and 2, respectively; h_w is the head loss between Sections 1 and 2; ξ_c is the local head loss coefficient; A is the cross-sectional area of the gate; v is the average velocity of water flow passing through the gate; ΔP the average pressure differential between Sections 1 and 2; Q is the flow rate of the gate.

To study the flow characteristics of the gate, the discharge coefficient of the gate is defined as follows:

$$K_v = \frac{A}{\sqrt{\sum \xi_c}} \sqrt{2}. \tag{7}$$

According to (6), the discharge coefficient of the gate can be written as

$$K_v = Q\sqrt{\frac{\rho}{\Delta P}}. \tag{8}$$

In this study, the gate was located in a pressurised channel. The discharge coefficient can be used to characterise the gate flow capacity. The larger the discharge coefficient, the better the discharge performance of the gate. The discharge coefficient of the gate is related to the flow rate in the channel, the pressure differential before and after the gate, and the fluid density. The discharge coefficients of the different water level differences at different openings were calculated using the flow velocity and pressure values before and after the gate.

The discharge coefficient was calculated using experimental data, and the curve was plotted as shown in Figure 5b. The discharge coefficients of the gate under the same opening were very similar under different working conditions. This also indicates that the discharge coefficient was determined by the shape and structure of the gate and can be used to characterise its flow performance.

The discharge coefficient showed an exponential growth trend within the range of 0–90° stroke. When the gate opening was <40°, the discharge coefficient of the gate was small, and the change was relatively gentle. At this time, the effect of the flow regulation was not significant. When the gate opening was >60°, the resistance in the channel decreased, and the discharge coefficient suddenly increased. At this point, the flow-regulation function of the gate became prominent. In addition, the blue error band in Figure 4b represents the difference between the discharge coefficient and mean under different operating conditions. When the gate opening was between 10–70°, the standard deviation of the discharge coefficient under different operating conditions was $<9.5 \times 10^{-4}$ When the gate openings were 80° and 90°, the standard deviations were 0.0021 and 0.0048, respectively. This indicates that there was a significant error in the discharge coefficient when the gate opening was large. This may be because during the large-opening experiment, the flow rate in the channel was high, and the water level in the tank fluctuated greatly, making it difficult to maintain a constant water level. This led to a significant deviation in the calculated discharge coefficient.

The experimental and simulation results were compared. When the gate opening reached 90°, the deviation between the simulation results and the experimental results was close to 10%. It is speculated that when the gate is fully opened, a small pressure differential exists between the front and rear of the gate in the channel, resulting in pressure measurement errors. The overall simulation results were in good agreement with the experimental data, confirming the reliability and accuracy of the proposed numerical simulation method.

3.1.2. Establishment of Steady-State Flow Prediction Model

A flow scatter plot of the gate under different openings and water level differences is shown in Figure 6. As shown in Figure 5b, the discharge coefficient followed a Gaussian distribution. Combining Equations (6) and (8), the variation law of the gate flow can be represented in the form of the function of Equation (9).

$$Q = (a + be^{-\frac{(\theta-c)^2}{d}})\sqrt{g\Delta H}, \tag{9}$$

where Q is the flow rate of the gate; ΔH is the upstream and downstream water level difference; θ is the gate opening; coefficients a, b, c, and d are related to the gate structure.

By combining the scatter plot for fitting, the fitting curve Formula (9) was obtained, and the fitting surface is shown in Figure 6. The final fitting result has a standard deviation of 5.6148×10^{-6} and a variance of 0.99845. Three operating conditions were selected for the experiment, and a comparison of the experimental and predicted results is presented in Table 4. All the prediction errors were <7%. The fitting results were good and could be used to guide the flow control of the gate.

$$Q = (0.000149777 + 0.07847e^{-\frac{(\theta-106.68128)^2}{2491.9089}})\sqrt{g\Delta H} \tag{10}$$

Table 4. Comparison between experimental results and predicted results.

Working Condition Group	Experimental Result/m^3·s^{-1}	Prediction Results/m^3·s^{-1}	Prediction Error
ΔH = 0.3 m, θ = 20°	0.00645	0.006854	6.27%
ΔH = 0.5 m, θ = 50°	0.04715	0.048181	2.17%
ΔH = 0.7 m, θ = 80°	0.15400	0.154845	0.55%

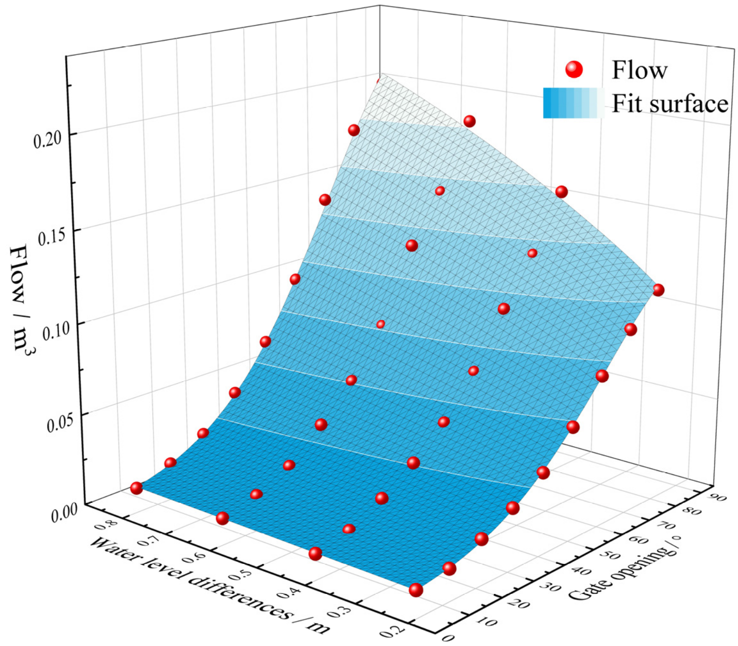

Figure 6. Flow rate fitting surface at different openings and water level differences.

3.2. Analysis of Steady-State Flow Field Characteristics

3.2.1. Flow Velocity Distribution Characteristics of Steady-State Flow Field

The selected operating conditions were a water level difference of 0.85 m, an inlet pressure of 11.27 kPa, and an outlet pressure of 2.94 kPa for analysis. The x-z cross-section within the water channel was selected for the analysis. The flow characteristics near the gate are clearly illustrated in Figure 7.

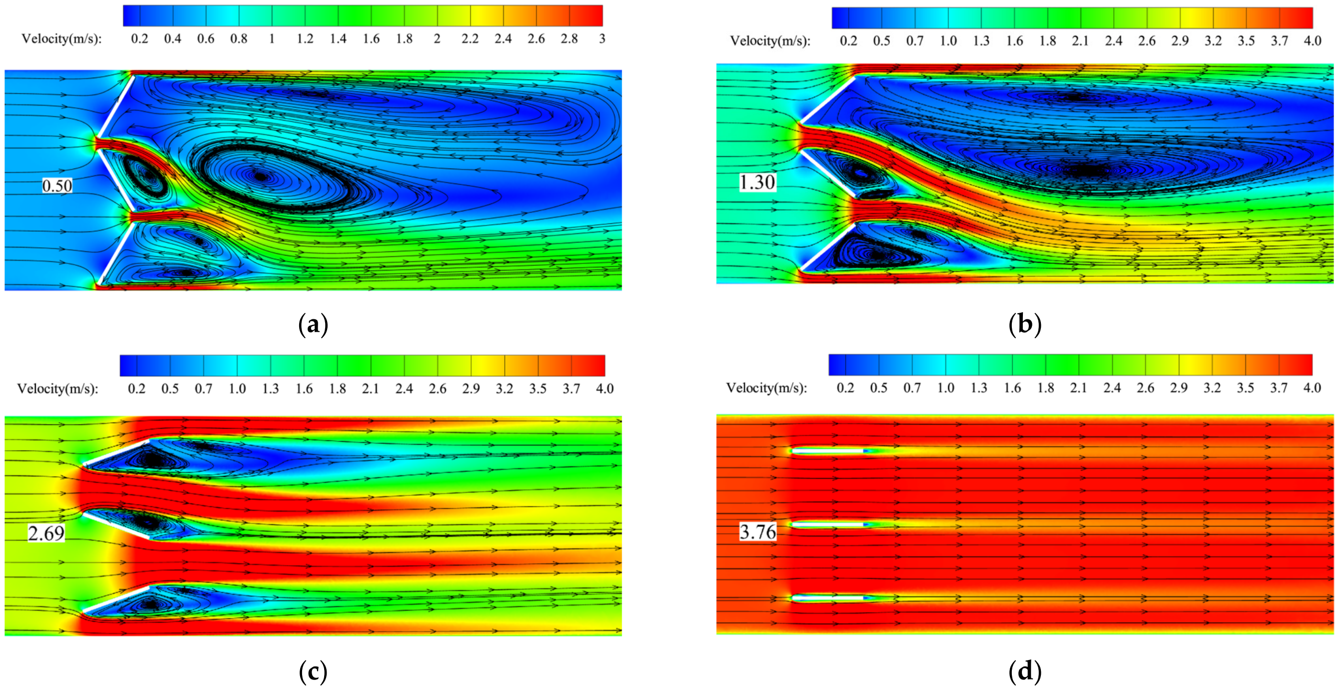

(**a**) (**b**)

(**c**) (**d**)

Figure 7. Velocity contour plots at different gate opening degrees: (**a**) 30°, (**b**) 50°, (**c**) 70°, and (**d**) 90°.

As shown in Figure 7a,b, when the gate opening was small, a jet phenomenon occurred when water flowed through the gate. The jets formed by different gates interfered with and deviated from each other. This resulted in the formation of complex asymmetric eddies downstream of the gate. The vortex was mainly distributed on the backflow surface of the gate and the downstream recirculation zone. As the gate opening changed, the centre of the vortex in the recirculation zone moved accordingly. The range and intensity of the vortices gradually decreased. As shown in Figure 7c,d, when the gate opening was >70°, the backflow zone disappeared. The vortex was distributed only on the backflow surface of the gate.

The flow velocity distribution curve along the route is shown in Figure 8. Under different opening degrees, there were significant differences in the distribution of flow velocity along the water channel at various positions owing to the influence of the gate opening shape. When the opening was constant, the flow velocity distributions at different positions upstream of the gate were consistent. From Figure 8a–d, the upstream velocities of the gate approach were 0.5, 1.3, 2.7, and 3.7 m/s, respectively. At different degrees of opening, the speed increased with the opening. As shown in Figure 8a–c, there was a significant change in the velocity at three locations around the horizontal axis of 1.0 m. When the fluid flowed through the gate, a smaller opening angle intensified the flow field changes in each profile and produced strong deviations in the transverse water surface profile. The velocities of the left and right lines increased to 4.38 m/s and 4.54 m/s, respectively, and eventually stabilised at 0.18 m/s and 0.77 m/s, respectively (Figure 8a). The velocities of the left and right lines increased to 4.80 m/s and 4.98 m/s, respectively, and eventually stabilised at 0.88 m/s and 1.74 m/s, respectively (Figure 8b). The velocities of the left and right lines increased to 5.39 m/s and 5.02 m/s, respectively, and eventually stabilised at 2.62 m/s and 3.02 m/s, respectively (Figure 8c). When the gate opening was small, the flow velocities of the three profiles showed a sharp increase owing to the generation and displacement of the jet phenomena. Subsequently, it decreased and generated a reflux. Finally, it gradually stabilised. The maximum flow velocity occurred at different cross-sections. The velocity of each section downstream of the gate varied owing to the different plate rotation directions. As shown in Figure 8d, when the gate opening was 90°, the gate was fully open, and an almost uniform transverse profile was observed downstream of the gate.

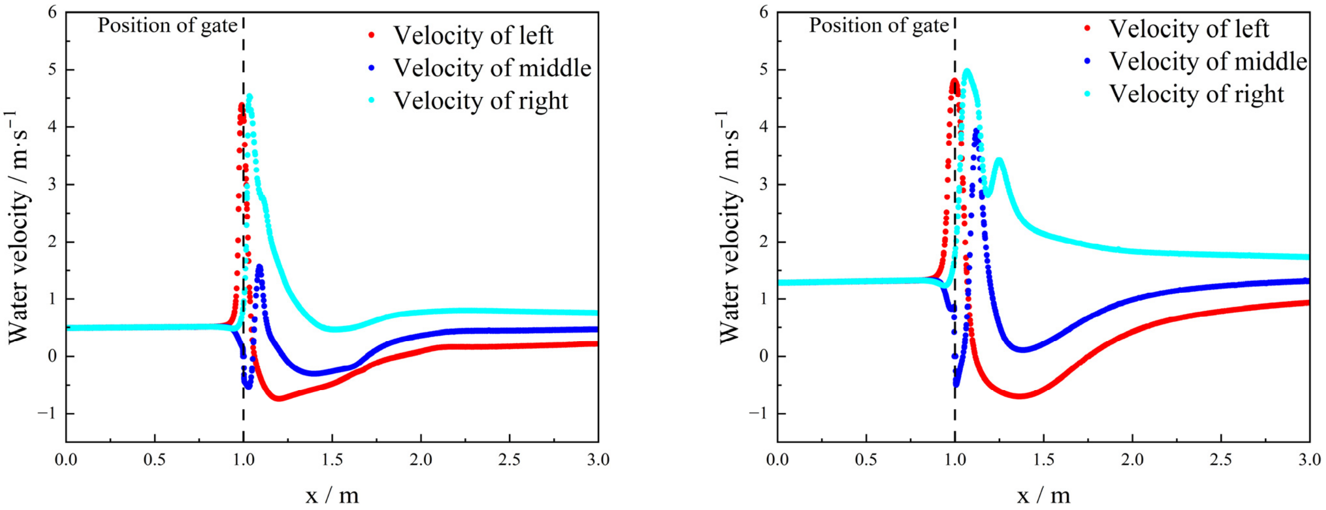

(**a**) (**b**)

Figure 8. *Cont.*

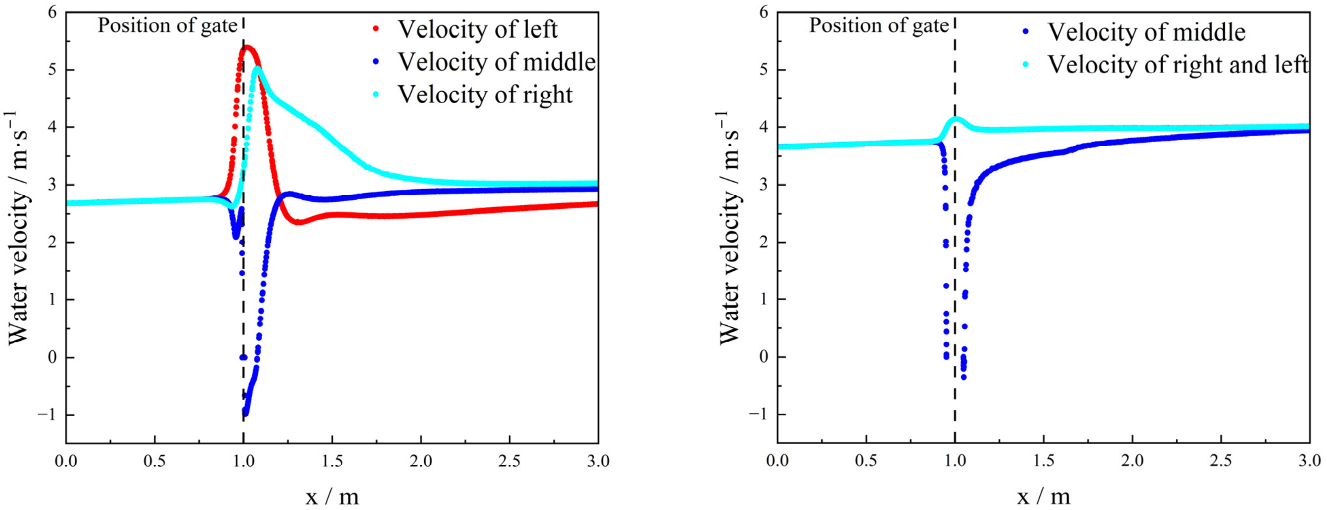

(**c**) (**d**)

Figure 8. Velocity distributions at different gate opening degrees: (**a**) 30°, (**b**) 50°, (**c**) 70°, and (**d**) 90°.

3.2.2. Pressure Distribution Characteristics of Steady-State Flow Field

The selected operating conditions were a water level difference of 0.85 m, an inlet pressure of 11.27 kPa, and an outlet pressure of 2.94 kPa for analysis. The pressure distribution curves along the three profiles at different openings are presented in Figure 9. When the opening remained constant, the pressure distributions at different positions upstream of the gate were essentially identical. From Figure 9a–d, the upstream pressures of the gate approached 11.14, 10.40, 7.60, and 4.4 kPa, respectively. This observation shows that the pressure at the upstream inlet decreased with an increase in the gate opening. As shown in Figure 9a–d, there was a significant change in the pressure at three locations around the horizontal axis of 1.0 m. The pressure change behind the gate was more severe. In Figure 9a, the pressures on the left, middle, and right lines decreased to minimums of 2.22, 0.50, and 1.50 kPa, respectively. In Figure 9b, the pressure on the left, middle, and right lines decreased to minimums of 0.24, −2.18, and −1.33 kPa, respectively. In Figure 9c, the pressure on the left, middle, and right lines decreased to minimums of −2.93, −4.98, and −3.64 kPa, respectively. The minimum pressure decreased as the opening increased. The minimum pressure on the left line exceeded that on the right line, and the minimum pressure on the right line exceeded that on the centreline. Combining Figure 7a–c, vortices were more likely to occur behind the gate. Owing to the local losses of the gate, the pressure downstream of the gate decreased compared to the upstream pressure. As shown in Figure 9a–c, the upstream and downstream pressure differences were 8.24, 7.5, and 4.7 kPa, respectively. As the gate opening increased, the relative pressure difference decreased.

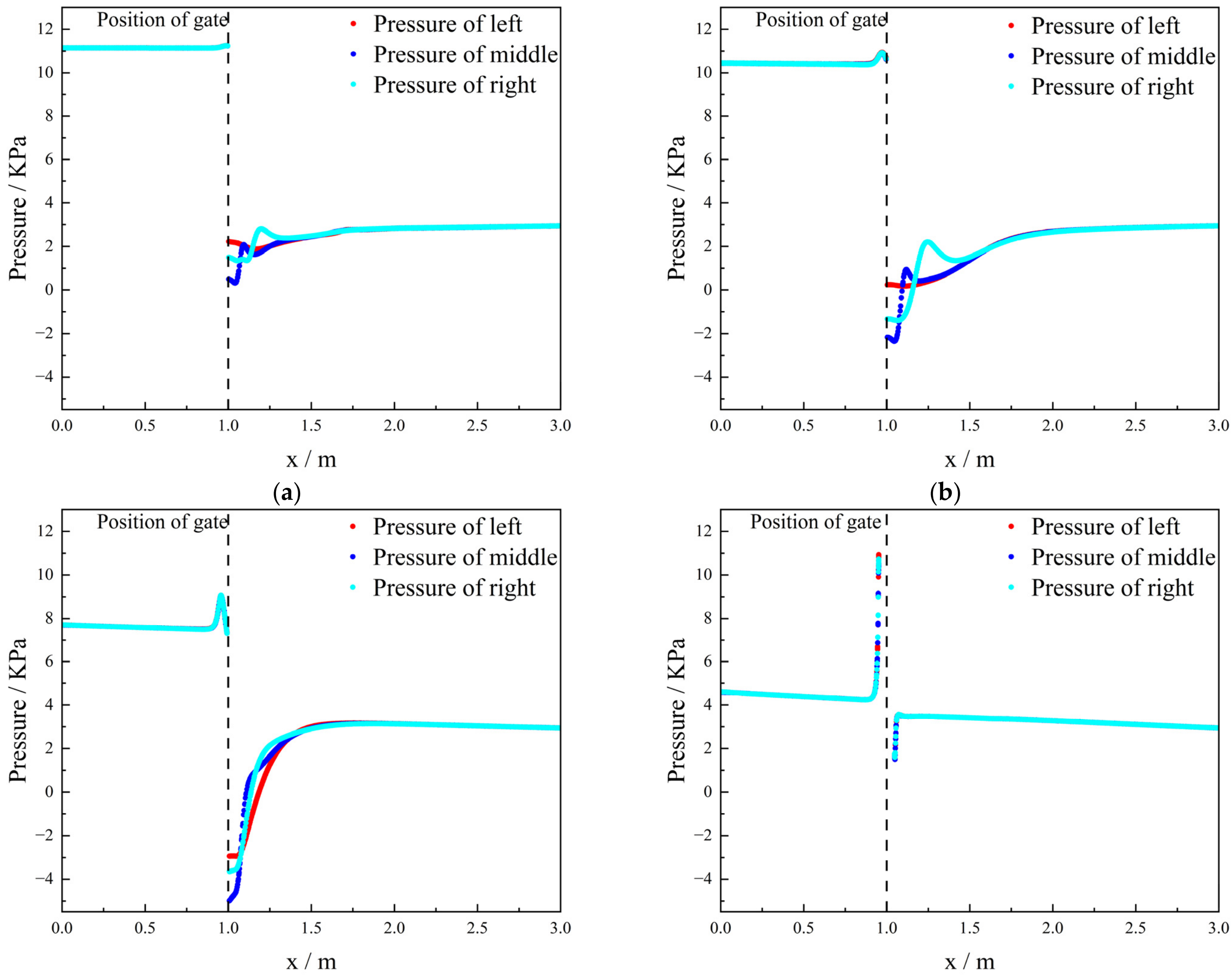

(**a**) (**b**) (**c**) (**d**)

Figure 9. Pressure distribution along different cross-sectional profiles at different opening degrees: (**a**) 30°, (**b**) 50°, (**c**) 70°, and (**d**) 90°.

3.2.3. Flow Force of Gates at Different Openings

The water flow forces acting on the walls of Plates 1, 2, and 3 in the x-axis direction are shown in Figure 10. When the gate opening was 10°, the forces acting on Plates 1, 2, and 3 were 159, 172, and 164 N, respectively, following the order Plate 2 > Plate 3 > Plate 1. Between the gate openings of 20° and 80°, the force on Plate 2 was greater than that on Plate 1, and the force on Plate 1 was greater than that on Plate 3. As the gate opening gradually increased, the pressure at the front of the gate plates gradually decreased. From 50° to 60°, the forces on Plates 1, 2, and 3 decreased by 22, 22, and 20 N, respectively. From 60° to 70°, the forces on Plates 1, 2, and 3 decreased by 40, 40, and 28 N, respectively. When the opening was greater than 60°, the rate of decrease in flow force significantly increased, which also indicated that the stress on the gate was greater when the opening was small. It was not until the opening was greater than 60° that the stress state significantly improved. When the gate opening was 80°, the forces acting on Plates 1, 2, and 3 were 34.67, 34.69, and 34.34 N, respectively. When the gate opening was 90°, the forces acting on Plates 1, 2, and 3 were 10.76, 10.66, and 10.81 N, respectively. When the gate opening was >80°, the flow forces acting on the three plates were almost equal. At this time, the flow inside the channel was good, and there was no interference between the three plates.

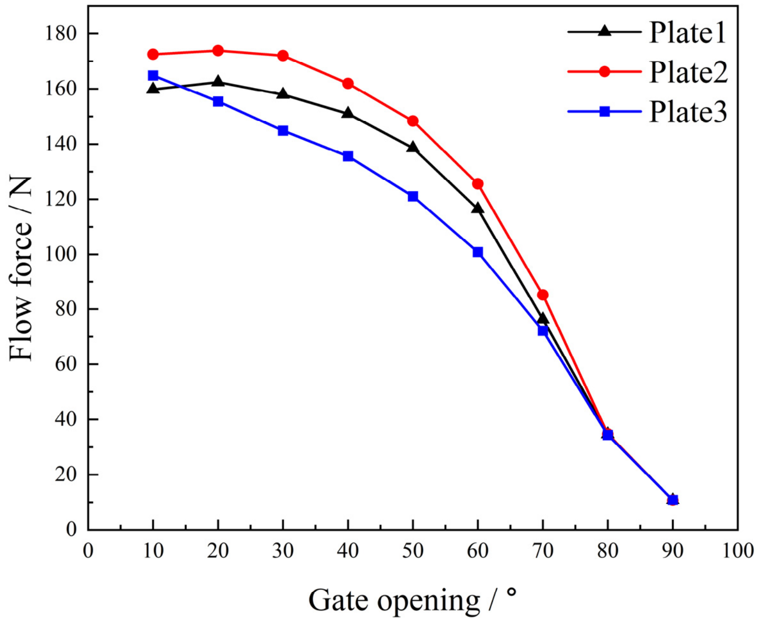

Figure 10. Flow forces on different plates.

To summarise the above, as the gate opening increases, the flow velocity increases, and the relative pressure difference decreases. The flow force acting on the plates gradually decreases during the gate-opening process. Moreover, the middle plate experiences the greatest flow force.

3.3. Analysis of Transient Flow Field Characteristics

3.3.1. Flow Velocity Distribution Characteristics

The gate plate is defined as an opening process between 0–90° and a closing process between 90–180°. A working speed of 100°/s was selected for analysis. As shown in Figure 11a–c, with a constant opening and closing speed of the gate, the vortex decreased as the gate continued to open. When the gate opening reached 90°, the vortex disappeared. From Figure 11c–f, as the gate gradually closed, the velocity difference in the channel increased, and the shear interaction between the fluids strengthened. Therefore, the number and intensity of vortices at the back of the gate further increased. The vortex mainly occurred in the corner vortex area on the backflow surface of the plate and the backflow area on the sidewall of the channel. Figure 12 shows that the maximum flow velocity occurred during the gate-closing process. The average flow velocity at the gate first increased and then decreased, and the rate of decrease in the flow velocity was faster.

As shown in Figure 12, during the opening process, the flow velocity in the channel was inversely proportional to the plate speed. The higher the plate speed, the smaller the average flow velocity of the channel cross-section. Under steady-state conditions, the flow velocity and flow rate in the water channel peaked at 3.65 m/s and 0.2189 m^3/s, respectively, at 90°. At a speed of 200°/s, the flow velocity and flow rate in the water channel peaked at 1.34 m/s and 0.0805 m^3/s, respectively, at 128°. At a speed of 100°/s, the flow velocity and flow rate in the water channel peaked at 1.99 m/s and 0.1199 m^3/s, respectively, at 118°. At a speed of 50°/s, the maximum flow velocity and flow rate in the water channel reached 2.67 m/s and 0.1599 m^3/s, respectively, at 110°. At a speed of 25°/s, the maximum flow velocity and flow rate in the water channel reached 3.18 m/s and 0.1906 m^3/s, respectively, at 103°. At a speed of 12.5°/s, the flow velocity and flow rate in the water channel peaked at 3.48 m/s and 0.2086 m^3/s, respectively, at 97°. When the speed decreased to 12.5°/s, the average flow velocity of the cross-section was close to the steady-state calculation results. Comparing the maximum flow velocity generation positions at different rotational speeds, the higher the rotational speed, the more delayed the maximum flow velocity. Overall, the smaller the relative opening of the gate, the more vortices there were. For the same relative opening, the vortex was greater during the closing process than during the opening process.

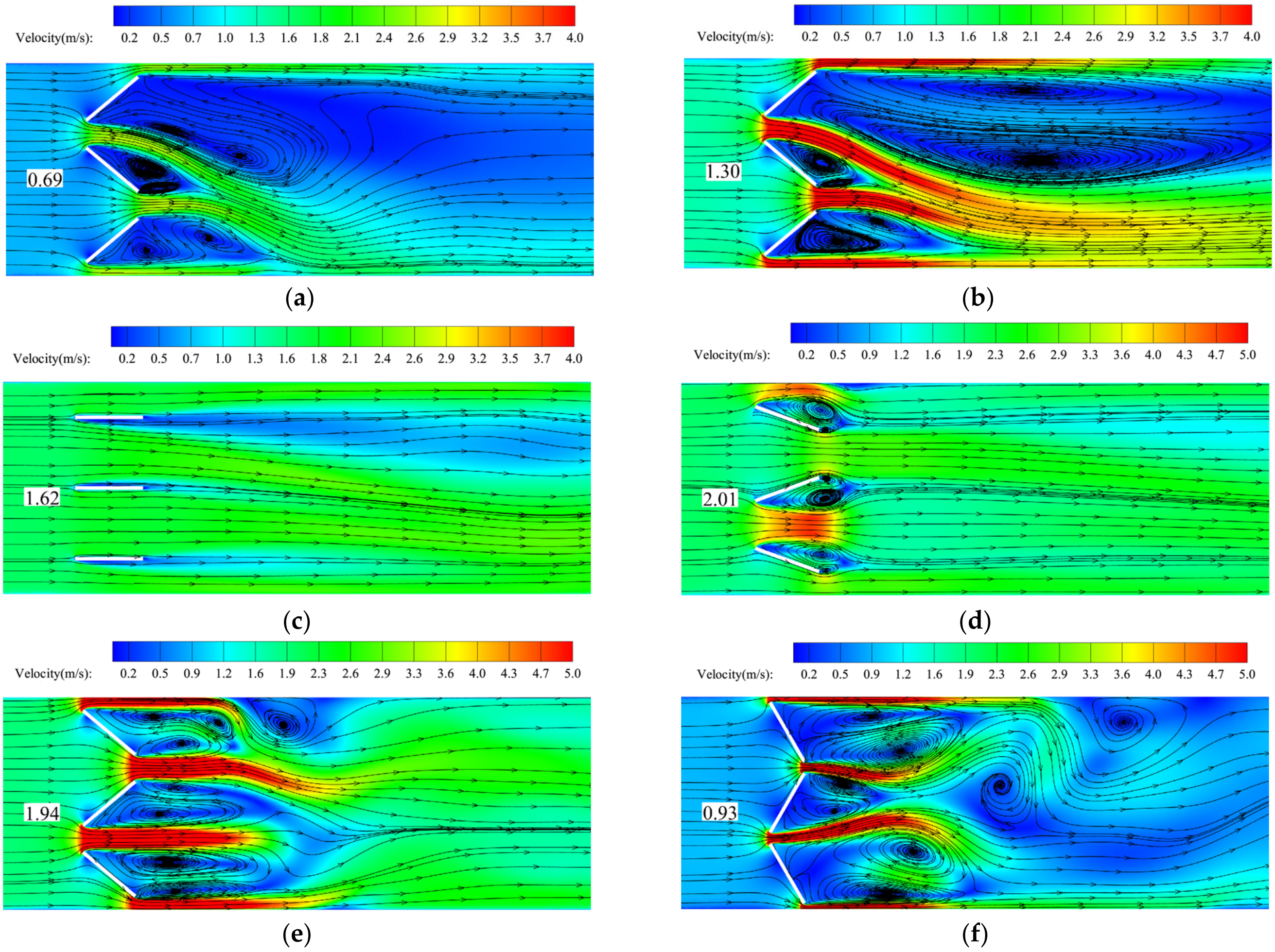

(**a**) (**b**)

(**c**) (**d**)

(**e**) (**f**)

Figure 11. Velocity contour plot of 100°/s operating conditions at different opening degrees: (**a**) 50°, (**b**) 70°, (**c**) 90°, (**d**) 110°, (**e**) 130°, and (**f**) 150°.

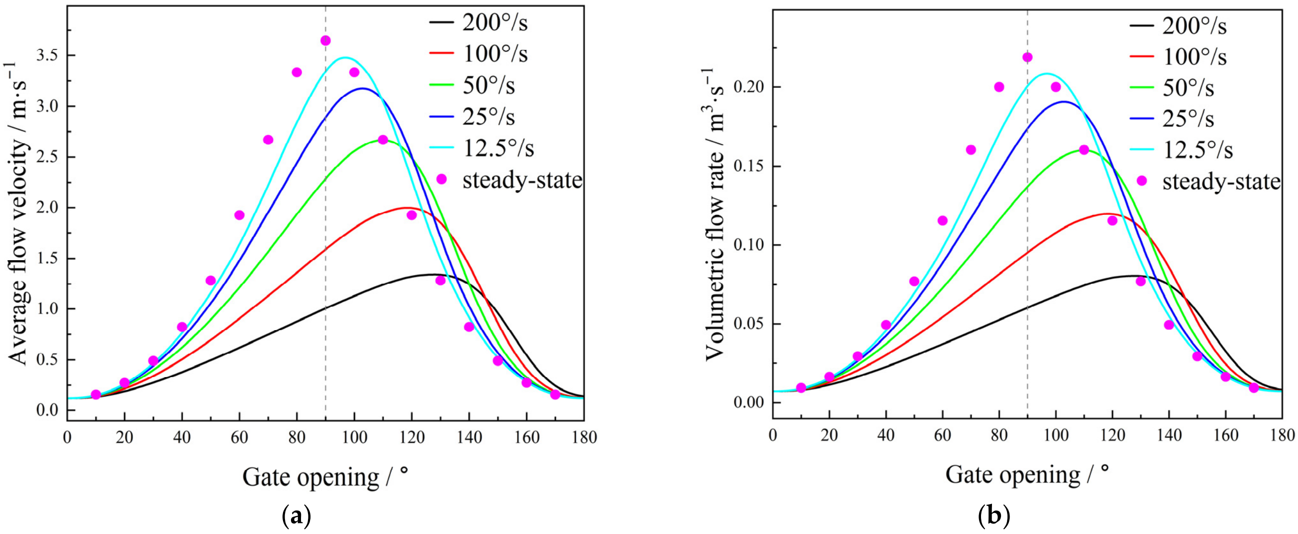

(**a**) (**b**)

Figure 12. Average flow velocity and volumetric flow rate curves at different speeds as a function of different gate opening degrees. (**a**) Average flow velocity, and (**b**) volumetric flow rate.

By monitoring physical quantities such as pressure, flow velocity, and flow rate during the transient calculation process, the discharge coefficient of the gate was obtained using Equation (4). A comparison between the transient and steady-state simulation results is shown in Figure 13. Within one opening and closing cycle of the gate, the discharge coefficient initially increased and then decreased. Under steady-state conditions, the discharge coefficient peaked at 0.1687 m^2 at 90°. At a speed of 200°/s, the discharge coefficient peaked at 0.0295 m^2 at 128°. At a speed of 100°/s, the discharge coefficient peaked at 0.0476 m^2 at 118°. At a speed of 50°/s, the discharge coefficient peaked at 0.0731 m^2 at 110°. At a speed of 25°/s, the discharge coefficient peaked at 0.1051 m^2 at 103°. At a speed of 12.5°/s, the discharge coefficient peaked at 0.1377 m^2 at 97°.

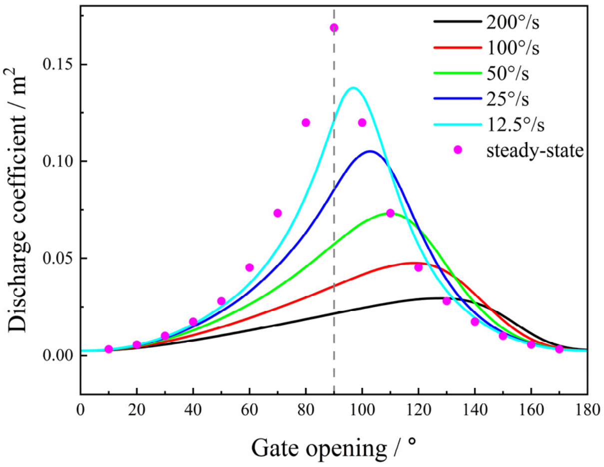

Figure 13. Discharge coefficient curves at different rotational speeds.

In the steady-state simulation, the maximum discharge coefficient was observed when the gate was fully opened. However, in the transient simulations, the changes in the discharge coefficient during the gate-opening and gate-closing processes did not exhibit a fully symmetrical pattern. The maximum value of the discharge coefficient did not occur when the opening of the gate was 90° but rather at a specific moment during the gate closing process. In addition, the faster the speed of the plate, the larger the gate opening corresponding to the position where the maximum value occurs. This suggests that initially, when the gate starts to close, the fluid's own inertia causes the rate of flow reduction to be slower than the rate of flow increase. Meanwhile, due to the influence of the rotating flow field of the gate, the flow field becomes smoother after an opening of 90°. This leads to an increase in the discharge coefficient after an opening of 90 degrees. As the fluid velocity and gate movement attain a state of dynamic equilibrium, the discharge coefficient peaks and subsequently begins to decline. This also resulted in the maximum discharge coefficient occurring after the opening of 90°. The discharge coefficient shows an asymmetric change.

We also observed variations in the discharge coefficients at different speeds. The slower the speed of the gate, the greater its maximum discharge coefficient. This value was close to the steady-state simulation results. The peak discharge coefficient increased by approximately 4.7 times at a gate speed of 12.5°/s compared to that at 200°/s. However, under high-speed operating conditions, the discharge coefficient of the gate changed relatively smoothly during its movement. No significant changes in flow were observed within a single opening or closing cycle. At a certain moment during the gate-closing process, the discharge coefficient of the gate with a speed of 200°/s exceeded that under the low-speed operating condition.

Overall, during the gate-opening process, the discharge coefficient of the gate decreased with increasing opening speed. At the same degree of opening, the discharge coefficient in the transient simulation was smaller than that in the steady-state simulation. During the gate closure process, the discharge coefficient exhibited asymmetric characteristics. When the closing speed was high, the lag effect of the decrease in the discharge coefficient was significant.

3.3.2. Pressure Distribution Characteristics

Figure 14 shows the pressure cloud map at 100°/s. As shown in Figure 14a–c, with the continuous opening of the gate, the maximum pressure and pressure differential of the gate exhibited a trend of first decreasing and then increasing. As shown in Figure 14a–d, the edge of the plate in the direction of the water flow was more prone to high pressure. Comparing Figure 14a,b with Figure 14d,e, the pressure difference was small during the opening process and large during the closing process. Negative pressure occurs during the closing process. This is more likely to cause cavitation and damage the equipment.

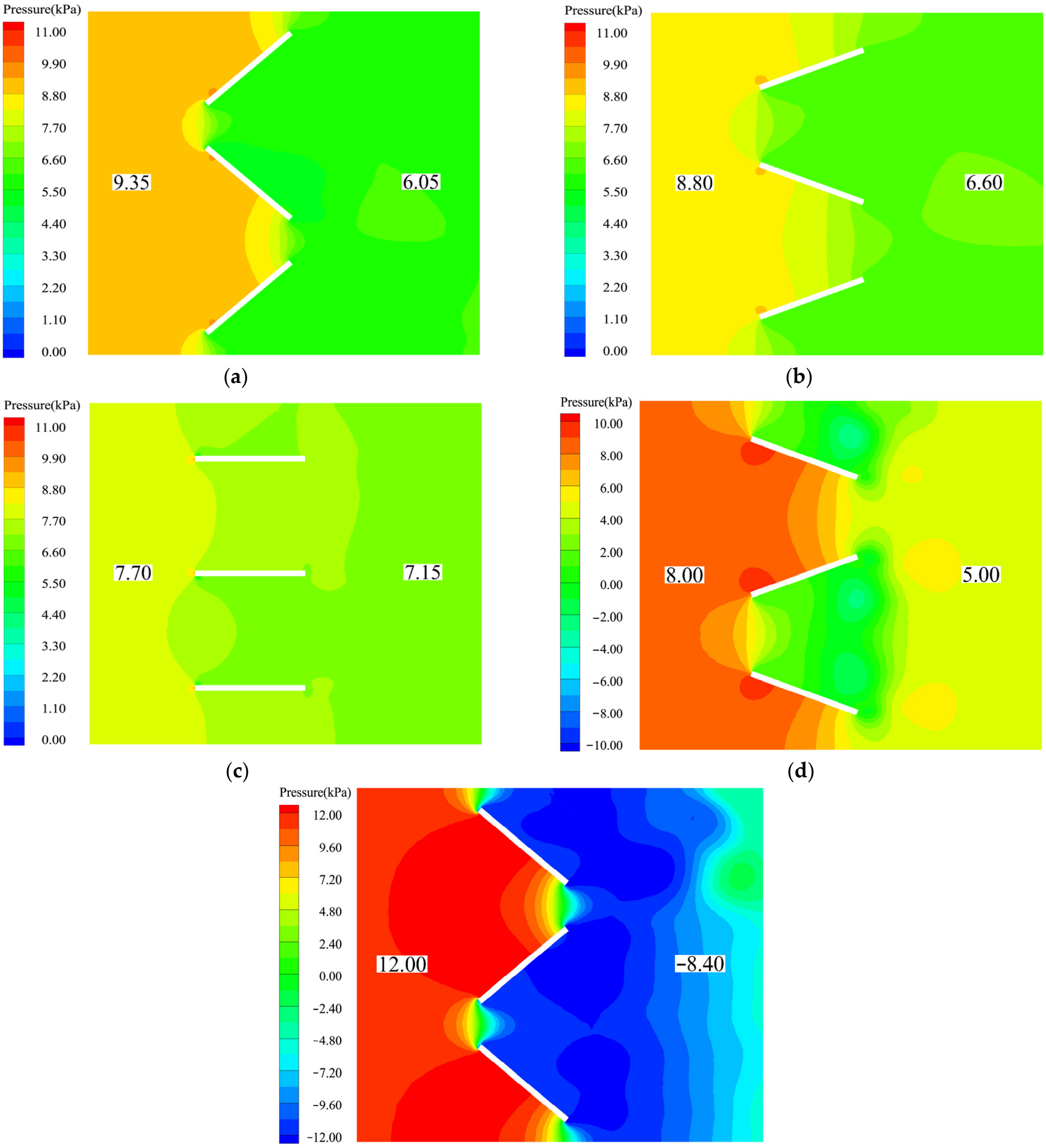

(**a**) (**b**) (**c**) (**d**) (**e**)

Figure 14. Pressure contour plots at different gate openings: (**a**) 50°, (**b**) 70°, (**c**) 90°, (**d**) 110°, and (**e**) 130°.

The variation law of the pressure differential was obtained by intercepting the pressure at both ends of the water channel, as shown in Figure 15. As shown in Figure 12, the locations of the extreme values of the pressure differential, flow rate, and flow coefficient were identical. Under steady-state conditions, the pressure differential peaked at 1682 Pa at 90°. At a speed of 200°/s, the pressure differential peaked at 7429 Pa at 128°. At a speed of 100°/s, the pressure differential reaches a minimum value of 6335 Pa at 118°. At a speed of 50°/s, the pressure differential peaked at 4779 Pa at 110°. At a speed of 25°/s, the pressure differential peaked at 3288 Pa at 103°. At a speed of 12.5°/s, the pressure differential peaked at 2293 Pa at 97°. The higher the rotational speed, the more delayed the minimum pressure differential. In addition, the pressure differential first decreased and then increased with an increase in the opening, and the rate of pressure differential increase was faster.

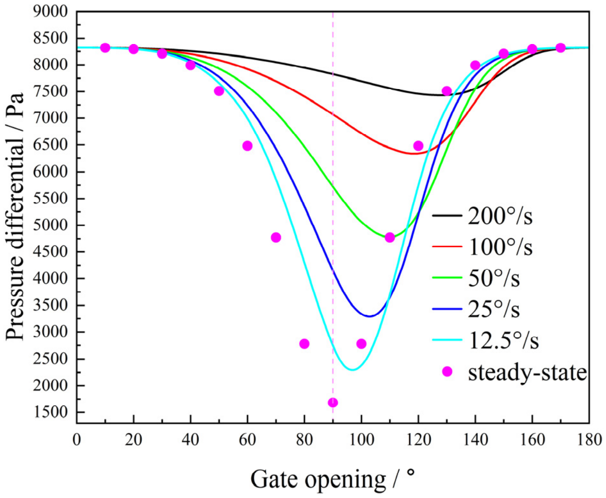

Figure 15. Pressure differential curves at different rotational speeds.

3.3.3. Flow Force of Gates During the Opening and Closing Process

The changes in the flow force experienced by the three plates are shown in Figure 16. As shown in Figure 16a–e, the flow force exerted on the plates gradually decreased during the gate opening process. When the gate opening was 90°, the force on the plate was close to zero. During the gate closure process, the flow force first increased sharply, peaked at a certain opening, and then decreased until it approached the initial flow force. Comparing Plate 2 in Figure 16a–e, the maximum stresses were 693, 516, 382, 269, and 205 N. The maximum forces occurred at 156°, 147°, 138°, 132°, and 130°, respectively. During the closing process, it was found that as the rotational speed decreased, the maximum flow force decreased, and the opening at which the maximum flow force was reached also became increasingly smaller.

When the speed of the gate was high, the three plates experienced almost the same trend in flow force changes, with differences only at the maximum value. In Figure 16a, the forces acting on Plates 1, 2, and 3 were 649, 693, and 660 N, respectively. In Figure 16c, the forces acting on Plates 1, 2, and 3 were 337, 382, and 331 N, respectively. Plate 2 experienced the maximum flow force, whereas Plates 1 and 3 experienced similar flow forces. This may be owing to the asymmetric distribution of vortices on the backflow surface of Plate 2. As the rotational speed decreased, the difference in the flow forces experienced by the three plates gradually increased. In Figure 16d, the forces acting on Plates 1, 2, and 3 were 225, 269, and 245 N, respectively. In Figure 16e, the forces acting on Plates 1, 2, and 3 were 169, 205, and 192 N, respectively. Overall, Plate 2 had the highest flow force, followed by Plate 3, whereas Plate 1 experienced the lowest flow force.

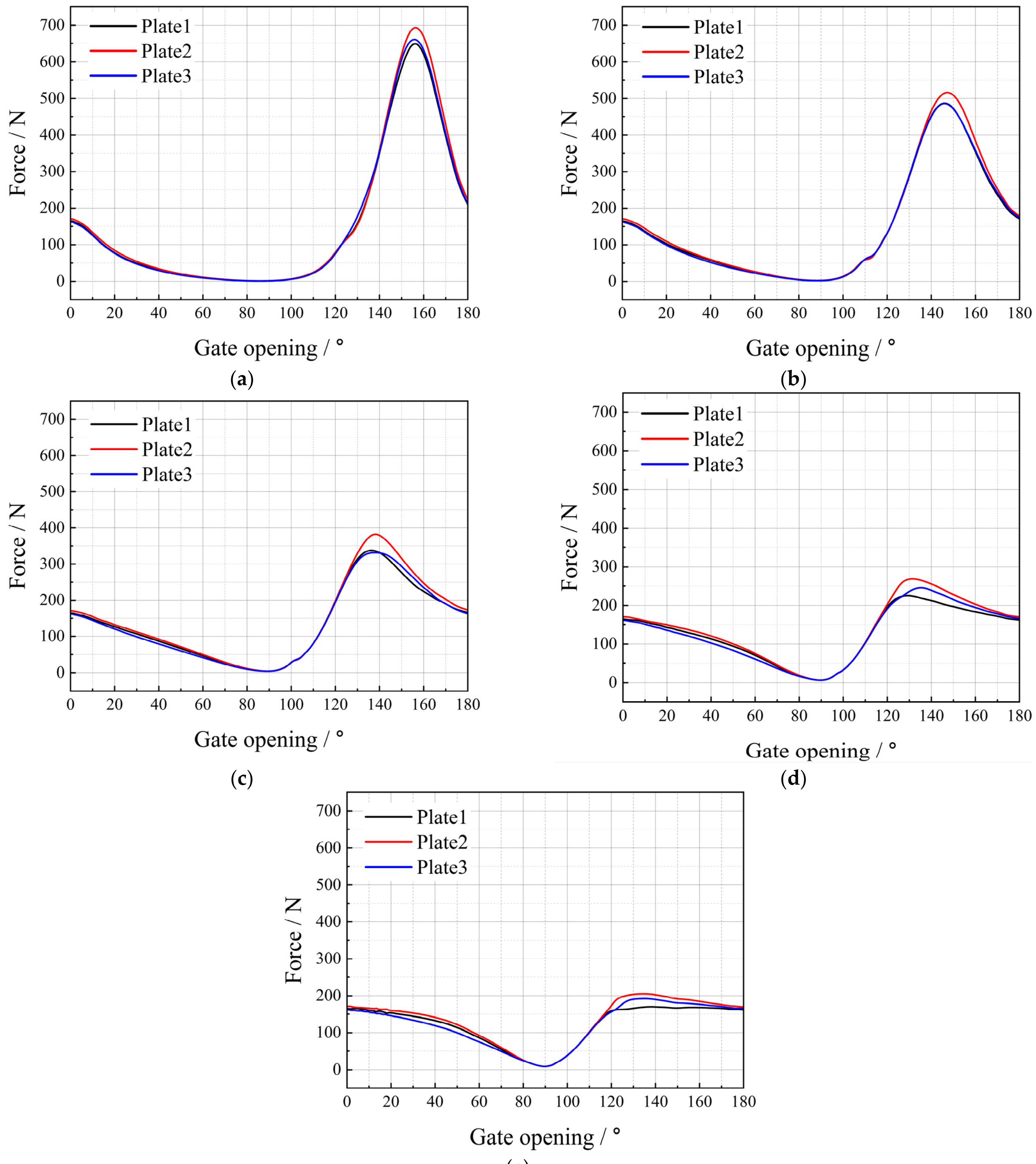

(**a**) (**b**) (**c**) (**d**) (**e**)

Figure 16. Flow force variations at different rotational speeds: (**a**) 200°/s, (**b**) 100°/s, (**c**) 50°/s, (**d**) 25°/s, and (**e**) 12.5°/s.

Overall, the flow force exhibited a periodic fluctuation pattern during the gate opening and closing processes. The flow force peaked at a certain opening during the gate-closing process, and the maximum flow force increased with increasing gate speed. In addition, as the rotational speed increased, the difference in the stress states of the three gate plates decreased.

To summarise the aforementioned points, the flow velocity, volumetric flow rate, and discharge coefficient of the gate increase first and then decrease with the increase in opening.

Conversely, the pressure differential initially decreases and subsequently increases. These parameters demonstrate asymmetric variation patterns, and the hysteresis effect becomes more pronounced at higher rotational speeds.

4. Conclusions

This study designed and developed a novel three-plate vertical rotary gate. The flow characteristics of the gate were investigated using model experiments. Considering factors such as the water level difference, gate opening, and gate opening and closing speed, steady-state and transient flow field simulations of the gate were conducted. The results can provide a reference for gate engineering applications. The specific research conclusions are as follows:

(1) Through model experiments on the gate, it was found that the discharge coefficient of the gate was consistent at the same opening, indicating that the discharge coefficient was determined by the shape and structure of the gate itself and can be used to characterise the flow performance of the gate. Within the opening range of 0–90°, the discharge coefficient of the gate exhibited an exponential growth trend. A steady-state flow prediction model was established that could be used for the flow control of the gates.

(2) Under steady-state conditions, the flow force acting on the plates gradually decreased during the gate opening process. Plate 2 experienced the highest flow force. The faster the plate speed, the greater the maximum flow force experienced. The gate discussed in this article involves a relatively small number of plates, and additional research is required to develop gates that are practical for real-world applications. When designing and applying the gate, it is necessary to consider strengthening the middle plates and reducing the plate speed.

(3) Under transient operating conditions, the discharge coefficient of the gate increased first and then decreased within the opening range of 0–180°. The discharge coefficients exhibited asymmetric characteristics. The higher the speed, the more obvious the hysteresis effect of the discharge coefficient. In the practical applications of such gates, the hysteresis effect should be considered for reasonable gate control.

Author Contributions: Methodology, H.Q. and Y.L.; validation, H.Q. and X.J.; formal analysis, H.Q.; investigation, H.Q.; resources, D.T., C.S. and Z.X.; writing—original draft preparation, H.Q.; writing—review and editing, X.Z. and Y.L.; visualisation, H.Q. and Y.S.; funding acquisition, X.Z. All authors have read and agreed to the published version of the manuscript.

Funding: This research was funded by the Natural Science Foundation of Shandong Province and the Taishan Industrial Experts Program, grant number ZR2022DKX001.

Data Availability Statement: The original contributions presented in this study are included in the article.

Acknowledgments: This work was supported by Natural Science Foundation of Shandong Province [grant numbers ZR2022DKX001] and Taishan Industrial Experts Program. These supports are appreciated.

Conflicts of Interest: Authors Xiao Zhang, Dong Tian, Chao Sun, and Zhenzhen Xue were employed by the company Shandong Fangneng New Growth Drivers Institute Co., Ltd. The remaining authors declare that the research was conducted in the absence of any commercial or financial relationships that could be construed as a potential conflict of interest.

References

1. Wang, Y.; Xu, G.; Li, W.; Liu, F.; Duan, Y. Characteristics of Plane Gate Vibration and Holding Force in Closing Process by Experiments. *Appl. Sci.* **2020**, *10*, 6111. [CrossRef]
2. Li, J.; Wang, C.; Wang, Z.; Ren, K.; Zhang, Y.; Xu, C.; Li, D. Numerical Analysis of Flow-Induced Vibration of Deep-Hole Plane Steel Gate in Partial Opening Operation. *Sustainability* **2022**, *14*, 3616. [CrossRef]

3. Wang, Y.; Xu, G.; Liu, Z.; Yang, D. Experimental Study on the Slip–Stick Vibration of Plane Gate. *Water* **2024**, *16*, 912. [CrossRef]
4. Zhonghao, Z.; Jiaxin, L.; Feng, F.; Xudong, Z. Selection of New Type Radial Steel Gate and Analysis of Static and Dynamic Characteristics. *Int. J. Steel Struct.* **2021**, *21*, 1630–1643. [CrossRef]
5. Xu, C.; Liu, J.; Zhao, C.; Liu, F.; Wang, Z. Dynamic failures of water controlling radial gates of hydro-power plants: Advancements and future perspectives. *Eng. Fail. Anal.* **2023**, *148*, 107168. [CrossRef]
6. Yu, Y.; Hong, Y.; Wang, S.; Ding, Z. Research on wear resistant bottom edge of radial gates. *J. Water Resour. Water Eng.* **2023**, *34*, 116–123.
7. An, Y.; Gu, R.; Cui, R.; Wu, P.; Ou, J. Nonlinear dynamic response analysis and assessment for miter gate subjected to ship impact. *Ocean Eng.* **2024**, *310*, 118799. [CrossRef]
8. Li, R.; Zhang, J.; Xiao, J. Operation State Evaluation of Miter Gate Based on On-Line Monitoring and Finite Element Analysis. *Appl. Sci.* **2022**, *13*, 381. [CrossRef]
9. Zhu, S.; Cheng, X. Test and analyses of a new double-arch steel gate under cyclic loading. *J. Constr. Steel Res.* **2008**, *64*, 454–464. [CrossRef]
10. Luo, Y.-Z.; Zhu, S.-Z.; Chen, X. Cyclic behavior test of a new double-arch steel gate. *J. Zhejiang Univ.-Sci. A* **2007**, *8*, 1731–1739. [CrossRef]
11. Liang, X.; Zhang, Q.; Huang, W.; Dai, Z.; Cai, J. Experimental and numerical study on static performance of ship lock sector gates. *J. Constr. Steel Res.* **2024**, *222*, 108977. [CrossRef]
12. Zhang, S.; Wang, X.; Ma, H. Operating Force Characteristics of Sector Gates Based on Prototype Testing. *Water* **2024**, *16*, 762. [CrossRef]
13. Seidel, C. Investigation of the Closing Operation of Emergency Sluice Gates and Their Influence on the Flow of Run-of-River Hydroelectricity. In Proceedings of the International Conference on Numerical Analysis and Applied Mathematics (ICNAAM-2018), Rhodes, Greece, 13–18 September 2018.
14. Wang, Y.; Xu, G.; Liu, F. Holding Force and Vertical Vibration of Emergency Gate in the Closing Process: Physical and Numerical Modelling. *Appl. Sci.* **2021**, *11*, 8440. [CrossRef]
15. Zhang, L.; Wang, Z.L.; Su, H.; Wang, X.Z.; Cao, Z.Y.; Zou, L.L. Influence of Gate Opening on Hydraulic Characteristics of Hydraulic Tunnel. *Water Resour. Power* **2023**, *41*, 117–120. [CrossRef]
16. Xu, C.; Wang, Z.; Zhang, H.; Li, H.; Li, D. Investigation on mode-coupling parametric vibrations and instability of spillway radial gates under hydrodynamic excitation. *Appl. Math. Modell.* **2022**, *106*, 715–741. [CrossRef]
17. Lee, S.O.; Seong, H.; Kang, J.W. Flow-induced vibration of a radial gate at various opening heights. *Eng. Appl. Comput. Fluid Mech.* **2018**, *12*, 567–583. [CrossRef]
18. Bijankhan, M.; Ferro, V.; Kouchakzadeh, S. New Stage-Discharge Relationships for Radial Gates. *J. Irrig. Drain. Eng.* **2013**, *139*, 378–387. [CrossRef]
19. Ferro, V. Simultaneous flow over and under a gate. *J. Irrig. Drain. Eng.* **2000**, *126*, 190–193. [CrossRef]
20. Shahrokhnia, M.A.; Javan, M. Dimensionless stage-discharge relationship in radial gates. *J. Irrig. Drain. Eng.* **2006**, *132*, 180–184. [CrossRef]
21. Marashi, A.; Kouchakzadeh, S.; Rashidi, N.; Yonesi, H.A. Rotary gate: Submerged flow condition. *Flow Meas. Instrum.* **2021**, *81*, 102035. [CrossRef]
22. Marashi, A.; Kouchakzadeh, S.; Yonesi, H.A.; Torabi-Poudeh, H. Hydraulics of Rotary Gate: Novel Structure for Semicircular Canals. *J. Irrig. Drain. Eng.* **2021**, *147*, 1537. [CrossRef]
23. Norouzi, R.; Ebadzadeh, P.; Sume, V.; Daneshfaraz, R. Upstream vortices of a sluice gate: An experimental and numerical study. *AQUA—Water Infrastruct. Ecosyst. Soc.* **2023**, *72*, 1906–1919. [CrossRef]
24. Elgamal, M.; Abdel-Mageed, N.; Helmy, A.; Ghanem, A. Hydraulic performance of sluice gate with unloaded upstream rotor. *Water SA* **2017**, *43*, 4. [CrossRef]
25. Kim, B.-J.; Hwang, J.-H.; Kim, B. FLOW-3D Model Development for the Analysis of the Flow Characteristics of Downstream Hydraulic Structures. *Sustainability* **2022**, *14*, 10493. [CrossRef]
26. Jung, J.-S.; Yoon, J.-S.; Kang, S.; Jeong, S.; Lee, S.O.; Park, Y.-S. Discharge Characteristics of Drainage Gates on Saemangeum Tidal Dyke, South Korea. *KSCE J. Civ. Eng.* **2021**, *25*, 1308–1325. [CrossRef]
27. Shen, C.; Wang, W.; He, S.; Xu, Y. Numerical and Experimental Comparative Study on the Flow-Induced Vibration of a Plane Gate. *Water* **2018**, *10*, 11551. [CrossRef]
28. Daneshfaraz, R.; Norouzi, R.; Ebadzadeh, P.; Kuriqi, A. Influence of sill integration in labyrinth sluice gate hydraulic performance. *Innov. Infrastruct. Solut.* **2023**, *8*, 1083. [CrossRef]
29. Daneshfaraz, R.; Norouzi, R.; Abbaszadeh, H.; Kuriqi, A.; Di Francesco, S. Influence of Sill on the Hydraulic Regime in Sluice Gates: An Experimental and Numerical Analysis. *Fluids* **2022**, *7*, 244. [CrossRef]
30. Enes, G.; Zeyneb, K.; Erdinç, İ.; Aydın, M.C. Investigation of the effect of variable-sized energy dissipating blocks on sluice gate performance. *Water SA* **2024**, *50*, 4064. [CrossRef]

31. Yan, X.; Wang, Y.; Fan, B.; Mohammadian, A.; Liu, J.; Zhu, Z. Data-driven modeling of sluice gate flows using a convolutional neural network. *J. Hydroinformatics* **2023**, *25*, 1629–1647. [CrossRef]
32. Daneshfaraz, R.; Norouzi, R.; Ebadzadeh, P.; Di Francesco, S.; Abraham, J.P. Experimental Study of Geometric Shape and Size of Sill Effects on the Hydraulic Performance of Sluice Gates. *Water* **2023**, *15*, 314. [CrossRef]
33. Rentachintala, L. Characteristics of discharge of skew side sluice gate. *J. Appl. Water Eng. Res.* **2024**, *14*, 1442. [CrossRef]
34. Meng, W.; Li, L.; Zhao, S.; Li, P. Flow regime discrimination and methodology for calculating discharge in trapezoidal sluice gates. *Flow Meas. Instrum.* **2024**, *100*, 102710. [CrossRef]
35. Wang, J.; Li, S.; Zhang, Y. Experimental and simulation analysis of flow patterns and energy dissipation through sluice gates in a U-shaped channel. *Water Supply* **2024**, *24*, 1393–1408. [CrossRef]
36. Shen, C.-Y.; Yang, R.-G.; Qing, S.; He, S.-H. Vortex analysis of water flow through gates by different vortex identification methods. *J. Hydrodyn.* **2023**, *35*, 112–124. [CrossRef]
37. Takagi, H.; Furukawa, F. Stochastic Uncertainty in a Dam-Break Experiment with Varying Gate Speeds. *J. Mar. Sci. Eng.* **2021**, *9*, 67. [CrossRef]
38. Li, S.; Wu, S.; Wang, X.; Li, G.; Li, H.; Lv, J.; Xie, J. Research on the response characteristics and operation control of unsteady water transport in Huangchigou water distribution hub. *Eng. Appl. Comput. Fluid Mech.* **2024**, *18*, 2398123. [CrossRef]
39. Zhang, R.; Shen, C.Y.; Ma, J.X. Time-frequency Characteristics Analysis of Pulsating Pressure of Water Flow Through Gate Based on Hilbert-Huang Transform. *Water Resour. Power* **2023**, *41*, 174–177. [CrossRef]
40. Li, D.; Wang, H.; Li, Z.; Nielsen, T.K.; Goyal, R.; Wei, X.; Qin, D. Transient characteristics during the closure of guide vanes in a pump-turbine in pump mode. *Renewable Energy* **2018**, *118*, 973–983. [CrossRef]
41. Tong, Z.; Yang, Z.; Huang, Q.; Yao, Q. Numerical Modeling of the Hydrodynamic Performance of Slanted Axial-Flow Urban Drainage Pumps at Shut-Off Condition. *Energies* **2022**, *15*, 1905. [CrossRef]
42. Wu, G.; Duan, X.; Zhu, J.; Li, X.; Tang, X.; Gao, H. Investigations of hydraulic transient flows in pressurized pipeline based on 1D traditional and 3D weakly compressible models. *J. Hydroinform.* **2021**, *23*, 231–248. [CrossRef]
43. Xie, C.; Fu, T.; Xuan, W.; Bai, C.; Wu, L. Optimization and Internal Flow Analysis of Inlet and Outlet Horn of Integrated Pump Gate. *Processes* **2022**, *10*, 1753. [CrossRef]